energies

MDPI

Article

Analysis of Energy Loss Characteristics in an Axial-Flow Reactor Coolant Pump Based on Entropy Production Theory

Zhong Li [1], Yanna Sun [1], Weifeng Gong [2], Dan Ni [1,*] and Bo Gao [1]

[1] School of Energy and Power Engineering, Jiangsu University, Zhenjiang 212013, China; lizhong@ujs.edu.cn (Z.L.); sunyanna253@163.com (Y.S.); gaobo@ujs.edu.cn (B.G.)
[2] Shanghai Marine Equipment Research Institute (SMERI), Shanghai 200031, China; wfgong1979@163.com
* Correspondence: nidan@ujs.edu.cn

Abstract: As the critical component of a nuclear power plant (NPP), the reactor coolant pump (RCP) will suffer energy losses during operation, which can lead to a series of safety issues and adversely affect the efficiency and stability of the NPP. In this study, the SST k-ω turbulence model is utilized to simulate the internal flow field of an axial-flow reactor coolant pump (RCP) under operating conditions of $0.8Q_N$ to $1.2Q_N$. Combined with entropy production theory, the distribution characteristics and hydraulic causes of energy loss within different regions of the RCP are revealed. The research findings are as follows: the total entropy production in the RCP first decreases and then increases during operation; with turbulent entropy production consistently accounting for over 70% of the total, and direct entropy production accounting for less than 10%. The impeller and annular casing are always the main components responsible for hydraulic losses within the pump. As the flow rate increases, the total entropy production in the impeller initially decreases and then increases, accounting for between 34.3% and 51% of the total; with energy losses mainly concentrated on the suction side of the impeller blades. The total entropy production in the annular casing gradually increases under operating conditions ranging from $0.8Q_N$ to $1.2Q_N$, accounting for between 20.4% and 50.3% of the total. Rotor-stator interaction (RSI), backflow, and flow separation near the volute tongue are significant causes of energy losses within the annular casing. Optimizing the geometric parameters of the impeller and annular casing is an effective way to reduce flow losses in axial-flow RCPs. The research results can provide a reference for the development of optimization techniques for RCPs.

Keywords: axial-flow reactor coolant pump; numerical simulation; entropy production theory; energy loss

Citation: Li, Z.; Sun, Y.; Gong, W.; Ni, D.; Gao, B. Analysis of Energy Loss Characteristics in an Axial-Flow Reactor Coolant Pump Based on Entropy Production Theory. *Energies* **2024**, *17*, 3399. https://doi.org/10.3390/en17143399

Academic Editor: Anton Vernet

Received: 2 June 2024
Revised: 5 July 2024
Accepted: 8 July 2024
Published: 11 July 2024

1. Introduction

As the international community is increasingly constrained by carbon emissions, nuclear energy—as a clean and efficient form of energy—has been widely used globally [1,2]. The reactor coolant pump (RCP) is the only rotating equipment within the pressurized water reactor (PWR) nuclear island, and its performance directly affects the operating efficiency and safety of the entire nuclear power plant (NPP) [3]. Compared with conventional pumps, the RCP adopts a large-scale annular casing in its hydraulic structure, which further increases the complexity of unstable flow within the pump, thereby causing significant energy loss. These losses not only reduce the operating efficiency of the RCP but may also trigger a series of safety issues, such as cavitation, vibration, and noise. Therefore, in the design and development process of the RCP, precise quantification analysis of its energy characteristics, identification of the main sources of energy loss, and the proposal of effective solutions are crucial for improving the operating efficiency of the RCP and the economic benefits of the NPP, and ensuring the safe and stable operation of the NPP.

Starting from the unsteady flow patterns within the RCP, it is one of the hot spots in this field to explore the improvement of stability and efficiency from the hydraulic factors.

Long et al. [4] and Xu et al. [5] analyzed the unsteady flow characteristics of pressure pulsations within a scaled-down model of an RCP under different inlet flow conditions, providing new insights for the optimization design of RCPs. Ye et al. [6,7] addressed the complex problem of energy conversion within various hydraulic components of the RCP under decelerating flow conditions. They obtained critical flow rate and speed data through experiments, established mathematical models to describe their temporal variations, and conducted detailed analyses of the hydraulic performance and vortex dynamics of the RCP during power outages at different time intervals. Tao et al. [8] investigated the internal flow characteristics of the nuclear main pump with an eccentric impeller using a combination of simulation and experimental methods, exploring the issue of flow-induced vibrations caused by impeller eccentricity. Lu et al. [9] simulated the distribution characteristics of internal flow velocity and turbulent kinetic energy of the main coolant pump under normal operating and accident conditions, providing references for the optimization of the main coolant pump and the lead-bismuth alloy cooling system. Ni et al. [10,11] measured the pressure pulsations within the RCP and, combined with detailed analyses of internal flow distribution using a Laser Doppler Velocimeter (LDV), revealed the unsteady flow mechanisms within the RCP. They also used large eddy simulation (LES) to study the correlation between the flow structure and pressure pulsations within the spherical casing. Yu et al. [12] analyzed the power loss of various hydraulic components of the RCP and found that, in non-uniform flow conditions, hydraulic losses mainly stem from the net reduction of mean kinetic energy.

In fluid machinery, accurately identifying and quantifying various types of flow losses within the flow field and establishing correlations between flow losses and flow structures are crucial for elucidating the mechanisms of flow losses. The entropy production method, as an effective tool for intuitively reflecting the locations of irreversible losses and energy consumption within fluid machinery, provides a novel approach for studying flow losses within fluid machinery [13–15]. Taha et al. [16] developed a novel elliptical coaxial ground heat exchanger using local entropy and heat exchange as optimization criteria. By comparing it with traditional circular coaxial ground heat exchangers, they explored the impact of key operational and design parameters on maximizing heat exchange and minimizing entropy generation. Wang et al. [17] analyzed the total entropy production and vortex volume fraction in a centrifugal pump under different cavitation conditions, revealing the mechanisms of irreversible flow losses caused by cavitation flow. Ji et al. [18] compared the energy loss characteristics of mixed-flow pumps with different tip clearances, focusing on the local entropy production caused by tip clearance leakage vortices. Yang et al. [19] validated the accuracy of the entropy production method in pump energy loss analysis and proposed an optimization model to improve the hump characteristics of large centrifugal pumps using total entropy production as the criterion. Li et al. [20] quantitatively evaluated the energy losses associated with vortex ropes in mixed-flow turbines using a local entropy production (LEPR) rate model, and visualized the position and intensity of the vortex ropes to gain a deeper understanding of vortex rope energy dissipation characteristics. Zhang et al. [21] applied the entropy production method to study the hydraulic losses in the front and rear chambers of centrifugal pumps operating as pumps and turbines; thereby gaining deeper insights into the performance and flow characteristics of centrifugal pumps. Sun et al. [22] effectively assessed the energy loss in turbine expanders dealing with cavitation flows of thermo-sensitive fluids by analyzing the time-averaged transport equations of entropy production rate. Mathi Muhammad et al. [23] investigated the entropy production problem in mixed convection of two Newtonian fluids under the presence of viscous and Joule dissipation, with the goal of minimizing entropy production.

In summary, the entropy production method has been widely applied across various fields, providing a powerful tool for the optimization of fluid machinery and in-depth research on fluid energy dissipation problems. This study investigates the complex flow structures within various hydraulic components of the axial-flow RCP model under differ-

ent operating conditions, aiming to uncover the distribution patterns of flow losses. The research conclusion can provide reference for further optimization of axial-flow RCP.

2. Experimental Setup

2.1. Model Pump

The subject of this study is a hydraulic scaled-down model (scale 1:2.866) of the axial-flow RCP used in the third-generation million-kilowatt PWR nuclear power unit "Hualong No.1" in China. Table 1 shows the main geometric parameters of the model pump used in this paper.

Table 1. The main geometric parameters of the model RCP.

Parameter	Value
Nominal head coefficient $\psi_N = \frac{2gH_N}{u_2^2}$	0.3522
Nominal flow rate Q_N	0.291 m^3/s
Nominal rotating speed n	24.75 s^{-1}
Specific speed $n_s = \frac{3.65n\sqrt{Q_N}}{H_N^{0.75}}$	502.5
Impeller blade numder Z_i	5
Guide vane blade numder Z_g	14
Impeller outlet diameter D_2	310.6 mm

2.2. Test Loop

A multi-functional closed-loop test rig for the model pump is constructed to meet the requirements of a hydraulic performance test. The experiment is conducted at the comprehensive performance test loop for the pump at the National Research Center of Pumps and Systems Engineering [24]. The test rig is illustrated in Figure 1a, with the model pump shown in Figure 1b. During the test, flow rate is measured using an electromagnetic flowmeter (accuracy ±0.5%). Two intelligent pressure transmitters (accuracy ±0.1%) are placed at a distance of twice the diameter of the pipe from the inlet and outlet flanges of the RCP to measure the pump head. The instantaneous speed and torque of the model pump are collected using a torque sensor (accuracy ±0.02%). In order to ensure high measurement accuracy, concentricity between the motor under testing, the model pump, and the sensors is maintained throughout the experiment. Real-time signals of power, torque, and speed are directly transmitted to a computer via the torque sensor to measure the efficiency of the pump.

In model testing, measurement accuracy is a crucial indicator of the precision of the results. To determine the total uncertainty of the test system, five groups of measurement data are collected under the same flow conditions. The average and standard deviation of these five sets of data are calculated. The random uncertainty and systematic uncertainty of each type of data are calculated according to relevant standards. The comprehensive uncertainty of the experiment was determined to be ±0.71%, demonstrating the reliability of the test results.

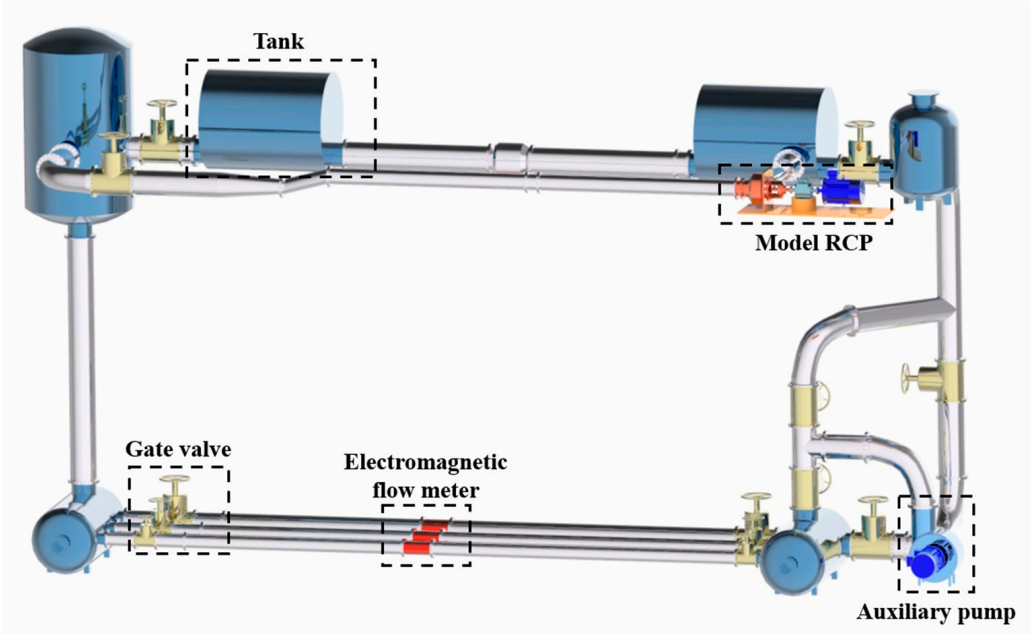

(**a**)

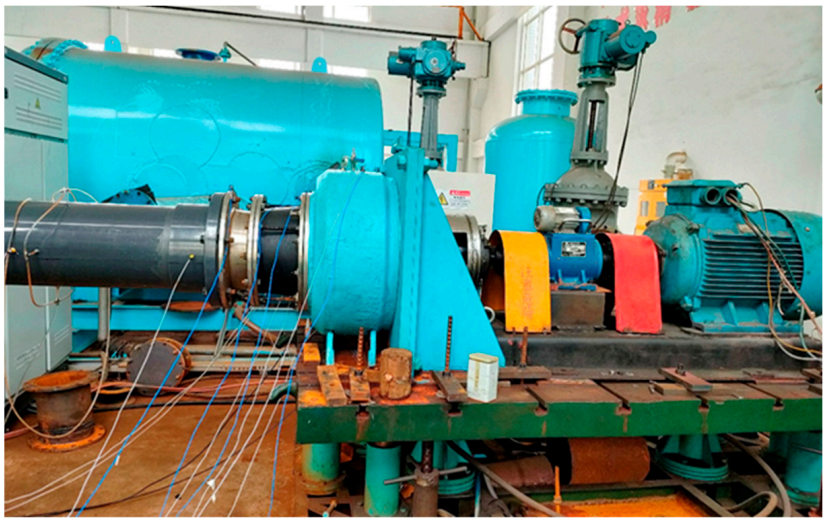

(**b**)

Figure 1. (**a**) Schematic diagram of the closed-loop test rig; (**b**) model pump.

3. Numerical Models and Schemes

3.1. Grid Generation and Independence Investigation

The hydraulic model of the RCP was developed, and the computational domain is divided according to the flow characteristics; as shown in Figure 2a. To enhance computational accuracy, hexahedral structured meshing was applied to all computational domains of the model pump. To ensure sufficient mesh precision and the ability to capture tip clearance leakage flow, local mesh refinement was implemented for the boundary layers of the hydraulic components and the tip clearance regions, as depicted in Figure 2b. This refinement ensures that the Y+ values of the impeller and guide vane blades meet the convergence requirements of the turbulence model under design conditions, with the Y+ value distribution shown in Figure 2c.

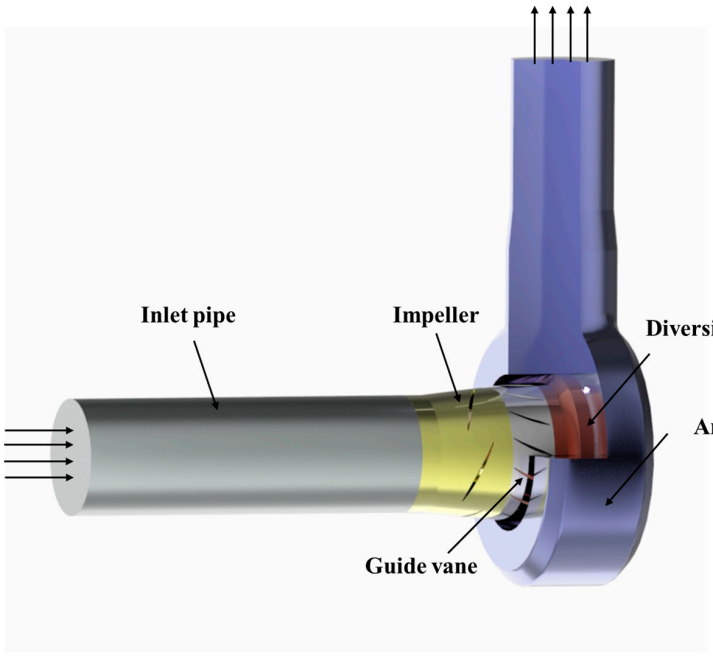

(**a**)

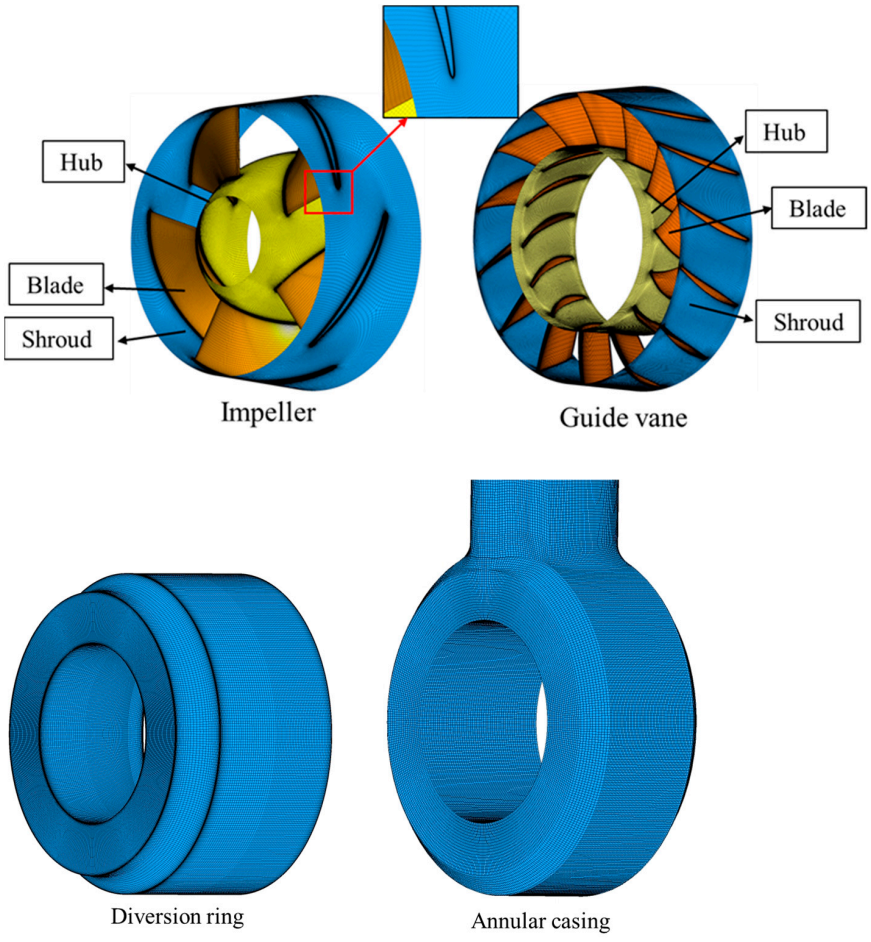

(**b**)

Figure 2. *Cont.*

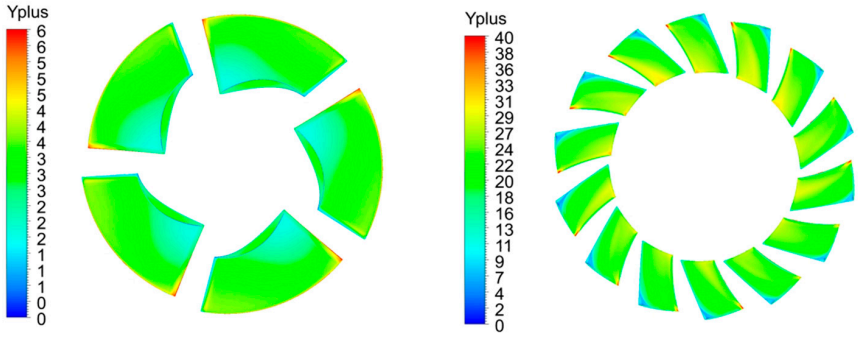

(**c**)

Figure 2. (**a**) Computational domain of the RCP; (**b**) structured grid of the RCP; (**c**) $Y+$ distribution on blades.

The number of model pump grids affects the precision of numerical simulation. Grid independence verification was conducted on the computational grid used, as shown in Table 2. By adjusting the division scale of the main flow region, five grid division schemes with different resolutions of the main flow region were designed. It can be seen from Table 2 that the nominal head coefficient of the model pump changes greatly when the number of grids is less than 12,025,308, and nominal head coefficient is less than 0.02% when it is higher than 12,025,308. To balance computational speed and efficiency, G4 was ultimately selected as the final grid calculation scheme.

Table 2. Grid independence verification.

Grid Division Schemes	Impeller	Guide Vane	Annular Casing	Total Number of Grid	Nominal Head Coefficient ψ_N
G1	2,390,378	2,005,362	1,208,217	5,891,146	0.3152
G2	3,137,922	2,744,391	1,296,881	8,019,064	0.3223
G3	3,579,664	3,079,582	2,280,308	10,178,081	0.3277
G4	4,261,031	3,721,019	3,203,765	12,025,308	0.3300
G5	4,721,186	4,103,503	3,891,407	14,563,195	0.3306

3.2. Boundary Conditions and Numerical Setting

The steady-state calculations for the RCP under various operating conditions were conducted using ANSYS CFX 19.0 software, with the steady-state results serving as the initial conditions for transient simulations. The shear-stress transport (SST) k-ω turbulence model was selected due to its combined advantages of both the k-ω and k-ε models in flow field simulation. The k-ω model is suitable for low Reynolds number calculations in near-wall regions, while the k-ε model has better adaptability for high Reynolds number calculations in free shear layers [25]. For the unsteady calculations, the transient rotor stator approach was employed to handle the interface between rotating and stationary domains. The boundary conditions were set as follows: the inlet boundary condition was specified as a total pressure inlet with a reference pressure of 1 atm; the outlet boundary condition was set as a mass flow rate outlet. All solid walls were set to no-slip boundary conditions, ignoring wall roughness effects, and the water temperature was set to 25 °C. In the transient calculations, the time step was set to 2.24467×10^{-4} s, corresponding to the time for the impeller to rotate by 2°. A total of 15 cycles were calculated, and the hydraulic performance results of the RCP were obtained by averaging the data from the last 5 cycles.

4. Entropy Production Theory

During the operation of the RCP, both the unstable flow in high Reynolds number regions and the viscous stress in the boundary layer led to an increase in irreversible

entropy, resulting in energy dissipation and a reduction in the hydraulic performance of the RCP. Assuming a constant internal temperature during operation, the total entropy production rate ($\dot{S}'_{pro,D}$) of the system is the sum of the local entropy production rate (LEPR) and the wall entropy production rate ($\dot{S}'_{pro,W}$) caused by wall effects. The LEPR is the sum of the direct entropy production rate ($\dot{S}'_{pro,\overline{D}}$) due to time-averaged velocity and the turbulent entropy production rate ($\dot{S}'_{pro,T}$) due to fluctuating velocity. The entropy production method is as follows [26].

$$\dot{S}'_{pro,D} = \dot{S}'_{pro,\overline{D}} + \dot{S}'_{pro,T} + \dot{S}'_{pro,W} \tag{1}$$

$$\dot{S}'_{pro,\overline{D}} = \frac{\mu}{T}\left\{2\left[\left(\frac{\partial \overline{u}}{\partial x}\right)^2 + \left(\frac{\partial \overline{v}}{\partial y}\right)^2 + \left(\frac{\partial \overline{w}}{\partial z}\right)^2\right] + \left[\left(\frac{\partial \overline{v}}{\partial x} + \frac{\partial \overline{u}}{\partial y}\right)^2 + \left(\frac{\partial \overline{w}}{\partial x} + \frac{\partial \overline{u}}{\partial z}\right)^2 + \left(\frac{\partial \overline{v}}{\partial z} + \frac{\partial \overline{w}}{\partial y}\right)^2\right]\right\} \tag{2}$$

$$\dot{S}'_{pro,T} = \frac{\mu}{T}\left\{2\left[\left(\frac{\partial u'}{\partial x}\right)^2 + \left(\frac{\partial v'}{\partial y}\right)^2 + \left(\frac{\partial w'}{\partial z}\right)^2\right] + \left[\left(\frac{\partial v'}{\partial x} + \frac{\partial w'}{\partial y}\right)^2 + \left(\frac{\partial w'}{\partial x} + \frac{\partial u'}{\partial z}\right)^2 + \left(\frac{\partial v'}{\partial z} + \frac{\partial w'}{\partial y}\right)^2\right]\right\} \tag{3}$$

In Equations (2) and (3), μ is the dynamic viscosity of the fluid; u, v, w are the three components of the local particle velocity in the Cartesian coordinate system; T is 298.15 K.

Due to the difficulty in obtaining turbulent velocity components, it is not possible to solve for the $\dot{S}'_{pro,T}$. Following the concepts proposed by Kock and Mathieu [27,28]—among others—when SST k–ω turbulence model is selected for calculation, the turbulent entropy production rate can be calculated by Formula (4).

$$\dot{S}'_{pro,T} = \beta\frac{\rho\omega k}{T} \tag{4}$$

In Equation (4), β = 0.09, ω is turbulent eddy viscosity frequency, K is turbulent kinetic energy.

The wall entropy production rate is defined as:

$$\dot{S}'_{pro,W} = \frac{\vec{\tau}\cdot\vec{v}}{T} \tag{5}$$

In Equation (5), τ is wall shear stress, v is velocity vector at the center of the first layer of grid cells in the wall region.

The total entropy production of the whole calculation domain is the sum of direct entropy production, turbulent entropy production and wall entropy production. The entropy production of each part can be calculated by integrating the entropy production rate.

$$S_{pro,\overline{D}} = \int_V \dot{S}_{pro,\overline{D}}dV \tag{6}$$

$$S_{pro,T} = \int_V \dot{S}_{pro,T}dV = \int_V \beta\frac{\rho\omega k}{T}dV \tag{7}$$

$$S_{pro,W} = \int_A \dot{S}_{pro,W}dA = \int_A \frac{\vec{\tau}\cdot\vec{v}}{T}dA \tag{8}$$

$$S_{pro,D} = S_{pro,\overline{D}} + S_{pro,T} + S_{pro,W} \tag{9}$$

In Equations (6) to (8), V is passing through fluid volume and A is passing through fluid area.

5. Result and Discussions

5.1. Hydraulic Performance Validation

The hydraulic performance validation results of the numerical simulation for the RCP are shown in Figure 3. Within the range of $0.8Q_N$ to $1.2Q_N$, the trend of the numerical simulation values is consistent with the experimental values, but they are generally lower than the experimental values. In the range of $0.8Q_N$ to $1.0Q_N$, the errors in the head coefficient and efficiency are relatively large; with maximum errors of 5.8% and 3.4%, respectively. At the design point ($1.0Q_N$), the errors in the head coefficient and efficiency are 3.4% and 0.1%, respectively. Overall, the results meet the requirements of engineering error. Therefore, the numerical calculation method and mesh adopted in this study can guarantee the dependability and accuracy of the results.

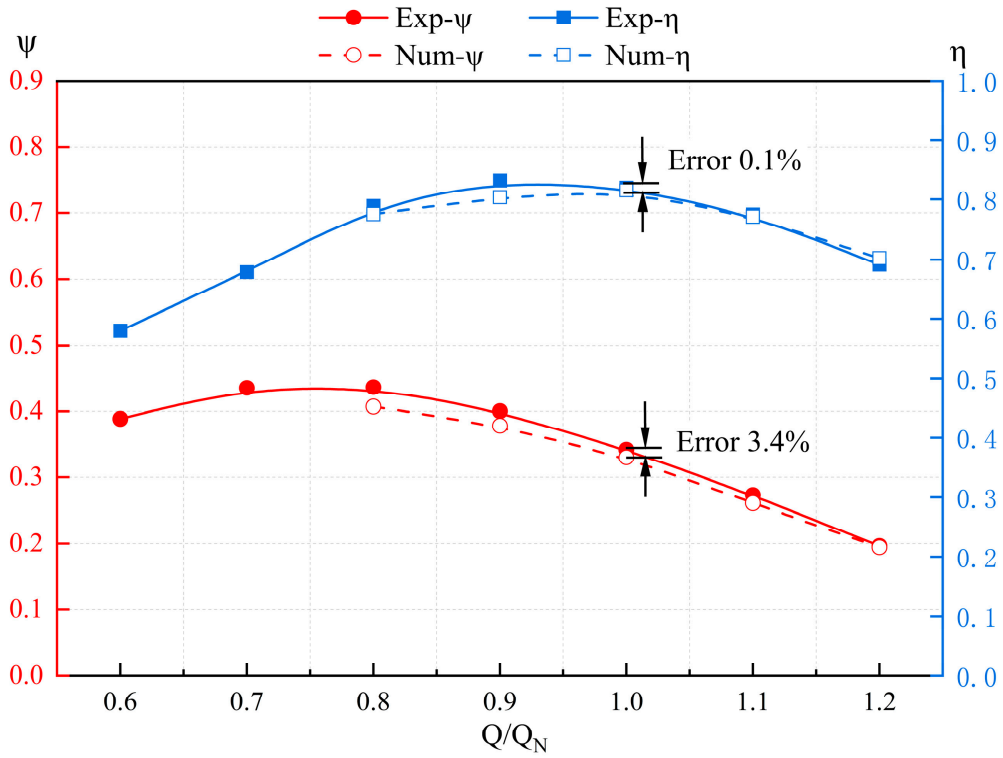

Figure 3. The hydraulic performance validation results of the RCP.

5.2. Entropy Production Characteristic Analysis

Figure 4 shows the validation results of hydraulic loss in the RCP calculated by entropy production theory. Ps represents the hydraulic loss calculated from the total pressure drop between the inlet and outlet of the RCP, while P_E represents the hydraulic loss obtained from experiments, which is calculated using Equation (10) [29]. The comparison reveals that the calculated values of Ps and $S_{pro,D}$ are always greater than those of P_E due to the omission of mechanical and volumetric losses in the numerical calculations. However, the trend observed across all three methods is consistent.

$$Hydraulic\ Loss = P - \rho gQH \tag{10}$$

The variation trends of the three types of entropy production in the entire flow region of the RCP with different flow rates are shown in Figure 4. As depicted in the figure, turbulent entropy production has the greatest contribution to the total entropy, accounting for more than 70% under each operating conditions. As the flow rate increases, turbulent entropy production shows a decreasing trend followed by an increase, reaching a minimum at $1.0Q_N$. Direct entropy production contributes the least to the total entropy production,

consistently accounting for less than 10%. With the increase in flow rate, the increase in time-averaged velocity gradients inside the pump leads to a slow increase in direct entropy production. The wall entropy production within the RCP accounts for 10% to 20%. As the flow rate increases, the velocity gradient caused by the shear force of the boundary layer gradually increases, resulting in a slow increase in wall entropy production.

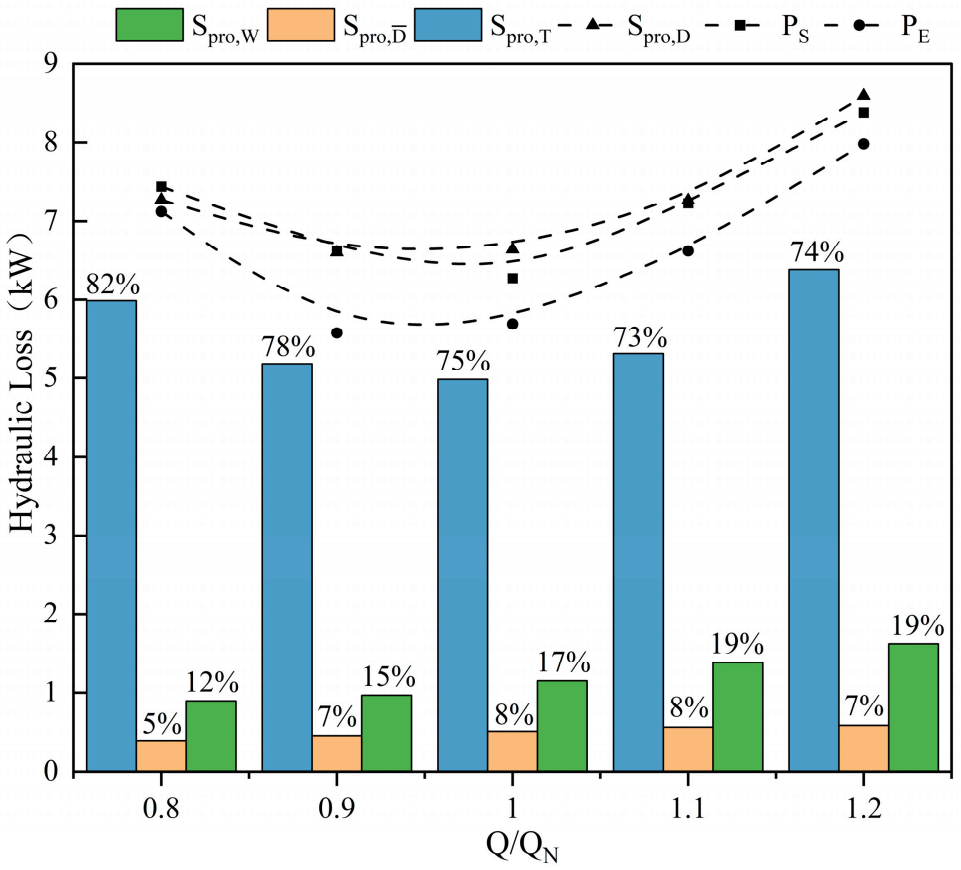

Figure 4. Three types of entropy production in the RCP and verification of entropy production theory.

The total entropy production values of various hydraulic components of the RCP under different operating conditions are shown in Figure 5, with the corresponding proportions illustrated in Figure 6. The hydraulic losses within the model pump mainly come from the annular casing and the impeller; followed by the guide vane, diversion ring, and inlet section. In the low flow rate range, the hydraulic losses within the RCP are mainly concentrated in the impeller; while in the high flow rate range, the hydraulic losses are mainly from the annular casing. Overall, with an increase in flow rate, the total entropy production within the annular casing gradually increases. The proportion of total entropy production within the annular casing sharply increases in the flow range of $0.8Q_N$ to $1.0Q_N$ and then shows a slow increase; with hydraulic losses in the annular casing accounting for 43.3% at the $1.0Q_N$. The proportion of total entropy production within the impeller undergoes a significant decrease in the flow range of $0.8Q_N$ to $1.0Q_N$, with a decreasing trend in the flow range of $1.0Q_N$ to $1.2Q_N$; and accounts for 38.9% of energy losses at the 1.0 Q_N. With the increase of flow rate, the total entropy production within the guide vane and diversion ring shows a steady decrease. The inlet section has the smallest proportion of hydraulic losses under all operating conditions, with minimal variation in flow rate.

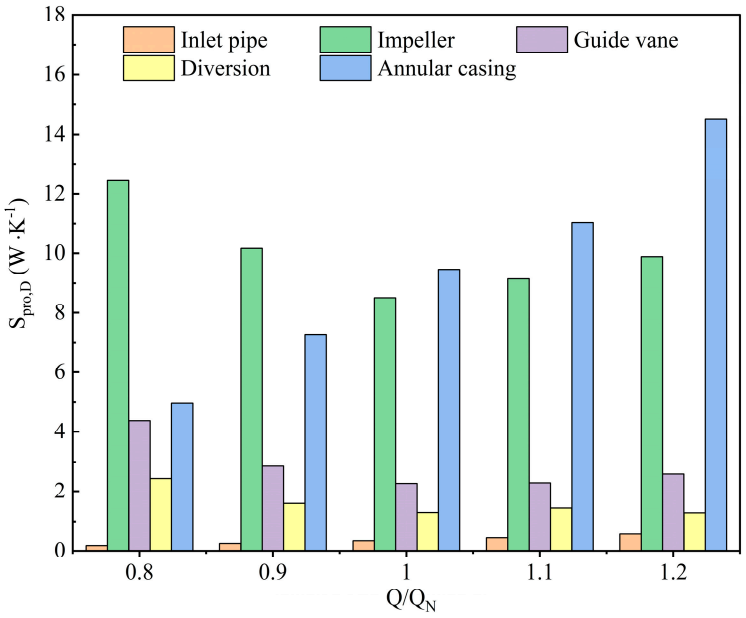

Figure 5. Total entropy production of various hydraulic components of the RCP.

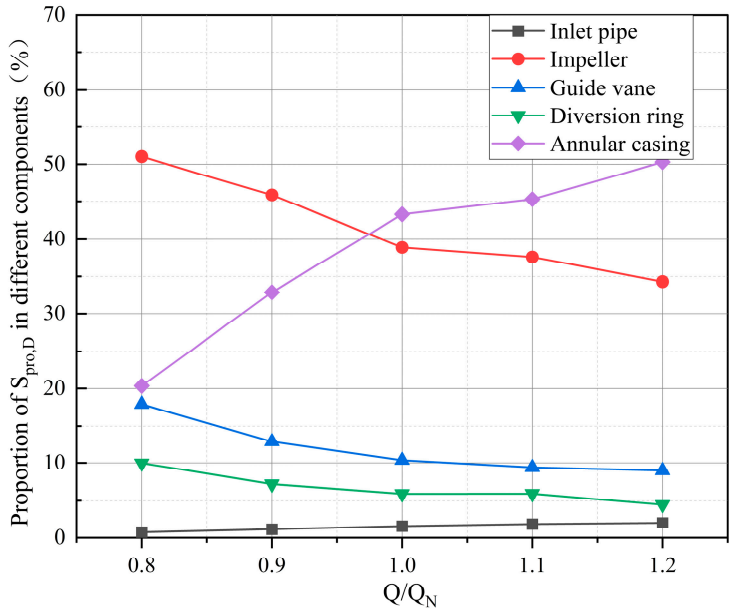

Figure 6. The proportions of total entropy production of various hydraulic components of the RCP.

5.3. Energy Loss Analysis

Based on the proportional characteristics of hydraulic losses of the RCP under various operating conditions, in order to further investigate the specific locations and magnitudes of hydraulic losses and their variation with flow rate, three representative operating conditions were selected: low flow condition ($0.8Q_N$), rated flow condition ($1.0Q_N$), and high flow condition ($1.2Q_N$). Energy loss analysis was conducted on each hydraulic component of the RCP under these conditions.

The analysis indicates that the guide vane and impeller are the components with relatively large hydraulic losses within the RCP. Therefore, cross-sections at three different span heights from the hub to the shroud of the impeller and guide vane (namely 0.05Span, 0.5Span, and 0.95Span) were selected. The LEPR on these cross-sections was analyzed in depth; as shown in Figure 7.

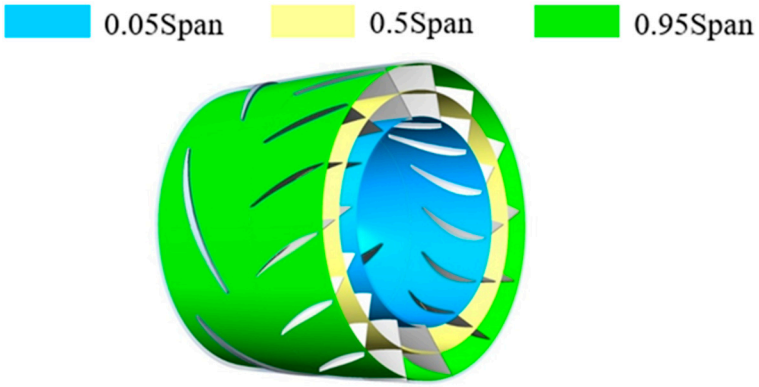

Figure 7. Cross-sectional diagram in the spanwise direction.

Figure 8 is the LEPR on different cross-sections of impeller and guide vane. As shown in the figure, the regions of high LEPR are mainly concentrated on the suction surface (SS) of the impeller blades, and the leading edge and wake regions of the guide vane blades. At the same flow rate, the area of high LEPR near the shroud is significantly larger than that near the hub. Additionally, hydraulic losses within the impeller and guide vane are greatest at $0.8Q_N$. As the flow rate increases, the disorder in regions of high LEPR decreases, and the area of these regions gradually reduces; extending from the leading edge to the trailing edge of the impeller and guide vane. Combining the streamline diagrams at different cross-sections under the three operating conditions (Figure 9), it is found that the scale of the unstable flow regions within the impeller and guide vane (the red circle dotted area) corresponds to the distribution of high LEPR. Under low flow rate conditions, fluid impacts the leading edge of the impeller blades. Due to the significant difference between the flow angle and blade setting angle, a large pressure difference is generated between the pressure surfaces (PS) and SS of the blades, causing flow separation and energy dissipation on the SS. With the increase of flow rate, the pressure difference between the PS and SS decreases, and the flow field stabilizes. At the 0.95Span cross-section near the shroud, large-scale backflow occupies the impeller passage due to tip clearance leakage flow and flow separation, accumulating substantial energy dissipation and reducing the hydraulic performance of the RCP. The hydraulic loss at the leading edge of the guide vane blades is caused by flow separation resulting from the misalignment between the fluid inflow direction and the blade leading edge. Notably, at the 0.05Span cross-section, flow separation occurs near the leading edge on the suction surface of the guide vane under low flow conditions. At $1.0Q_N$, the separation point moves towards the trailing edge of the guide vane; while under high flow conditions, the separation point concentrates on the PS.

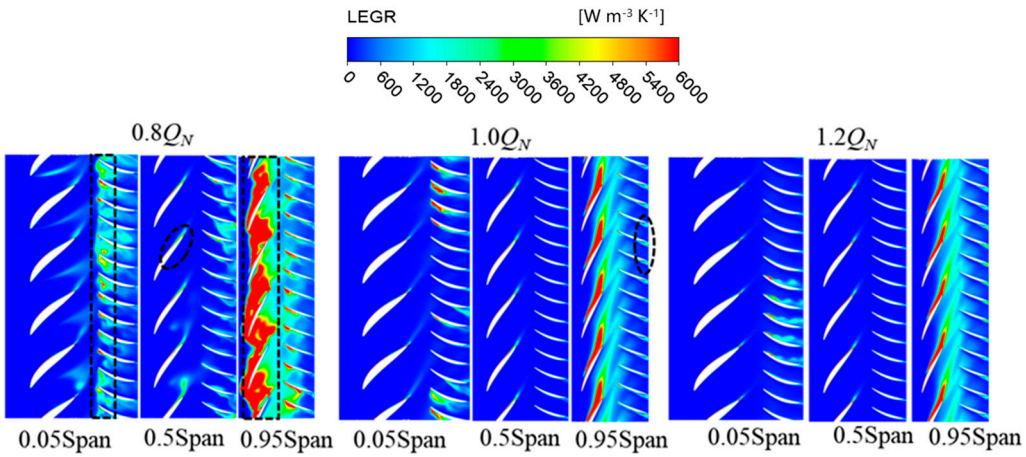

Figure 8. The LEPR of impeller and guide vane on different cross-sections.

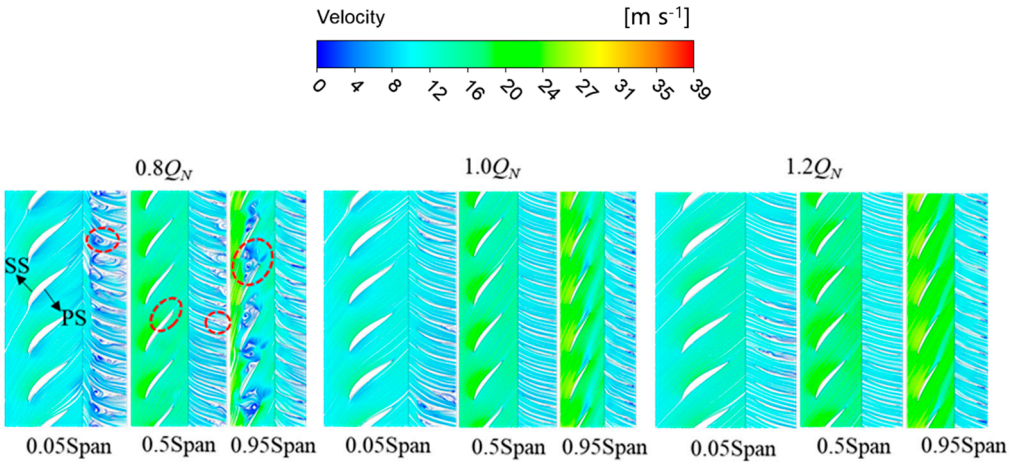

Figure 9. The streamline diagrams on different cross-sections of the impeller and guide vane under various flow rate conditions.

From the above analysis, it is evident that wall entropy production is also a significant component of energy loss within the RCP. To investigate its distribution pattern, the wall entropy production rates in various regions within the impeller and guide vane were analyzed. As shown in Figure 10a, the wall entropy production rate at the impeller outlet is significantly lower than at the inlet, and it gradually decreases from the shroud to the hub, displaying a gradient distribution. This is attributed to the increased wall shear stress in the shroud region due to tip clearance leakage flow. High wall entropy production rate areas are mainly concentrated near the leading edge of the blades. With the flow increasing from 0.8Q_N to 1.2Q_N, the wall entropy production rate gradually increases; extending from the leading edge to the trailing edge of the blades, with the area of high wall entropy production rate regions expanding. Figure 10b shows that high wall entropy production rate areas are primarily concentrated near the shroud at the guide vane inlet. With increasing flow rates, the wall entropy production rate in the guide vane initially decreases and then increases; while the wall entropy production rate on the shroud gradually decreases.

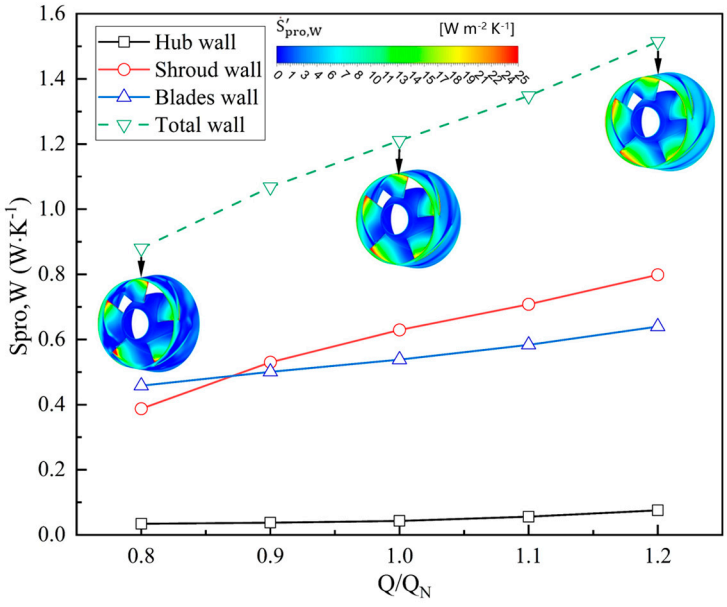

(**a**)

Figure 10. *Cont.*

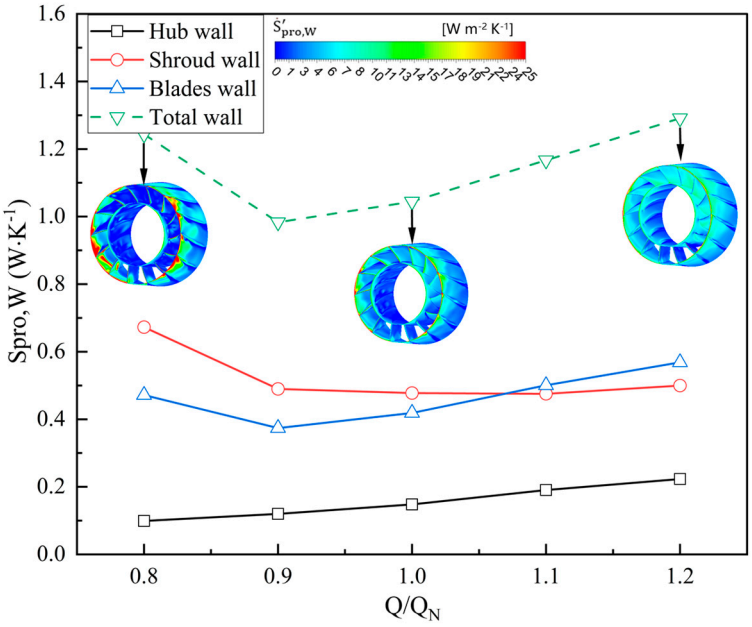

(**b**)

Figure 10. (**a**) Variation curve of wall energy loss in each area of impeller; (**b**) variation curve of wall energy loss in each area of guide vane.

To investigate the spatial distribution characteristics of energy loss within the annular casing of the RCP, the casing is divided into 12 regions as shown in Figure 11; denoted as V_i (i = 1,2...12). Figure 11 indicates that the distribution of energy loss across different regions exhibits significant non-uniformity at various flow rates. At $0.8Q_N$, the energy loss in the symmetrically left and right regions of the casing are almost equal. As the flow rate increases, energy losses in all regions increase, particularly in the right volute tongue region and the discharge pipe region. Overall, the energy loss on the right side of the annular casing is greater than on the left side.

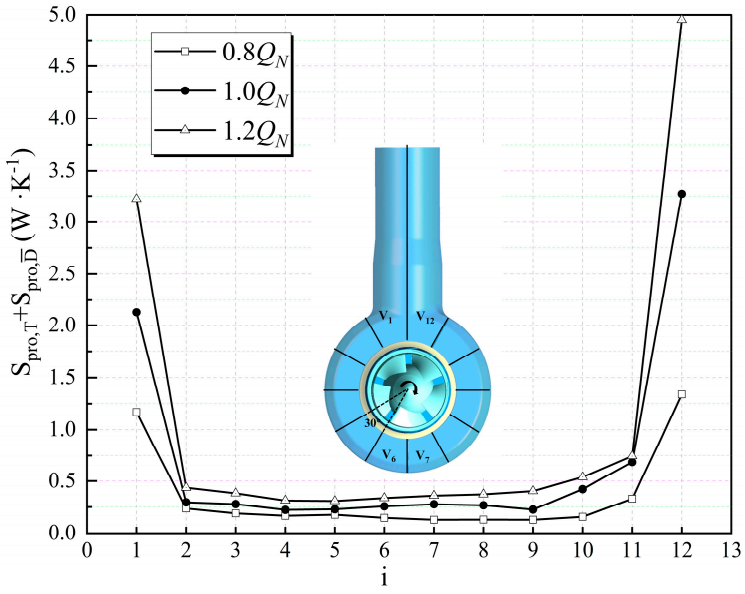

Figure 11. Distribution of local entropy production in annular casing under different operating conditions.

As illustrated in Figure 12a, the mid-plane of the annular casing—designated as Plane A—is selected for analyzing the energy loss within the annular casing based on the LEPR. Figure 12b shows the distribution of LEPR in plane A under different flow rates. Generally speaking, regions of high LEPR are mainly concentrated in the areas at the junction of the annular casing and the diversion ring (region A), near the right tongue and its surroundings (region B) and in the left tongue region (region C). The area of high LEPR near the volute tongue and discharge pipe increases significantly with the increase of flow rate, while the distribution of LEPR in the annular casing is uniform. Combined with the velocity streamline diagram on Plane A—as shown in Figure 13—significant differences in flow structures within the annular casing are observed under various operating conditions, with the eddies of different scales (see the red dotted area). Under the $0.8Q_N$ condition, the streamline distribution on Plane A is uniform; and energy dissipation occurs at region A due to the rotor-stator interaction (RSI) at the junction of the diversion ring and the annular casing. As the flow rate increases, the flow field inside the annular casing gradually becomes turbulent, with a significant increase in the number and scale of eddy currents. Near the right volute tongue, fluid entering the annular casing from the diversion ring impacts the right volute tongue area, causing a change in the flow direction. Part of the fluid flows into the discharge pipe along with the main flow, while another part continues to circulate within the annular flow region; interacting with the main flow and generating large scale vortices, resulting in energy dissipation in region B. When the fluid passes through the left volute tongue area, the flow separation occurs; which further increases the velocity gradient in this area and leads to the energy loss in region C.

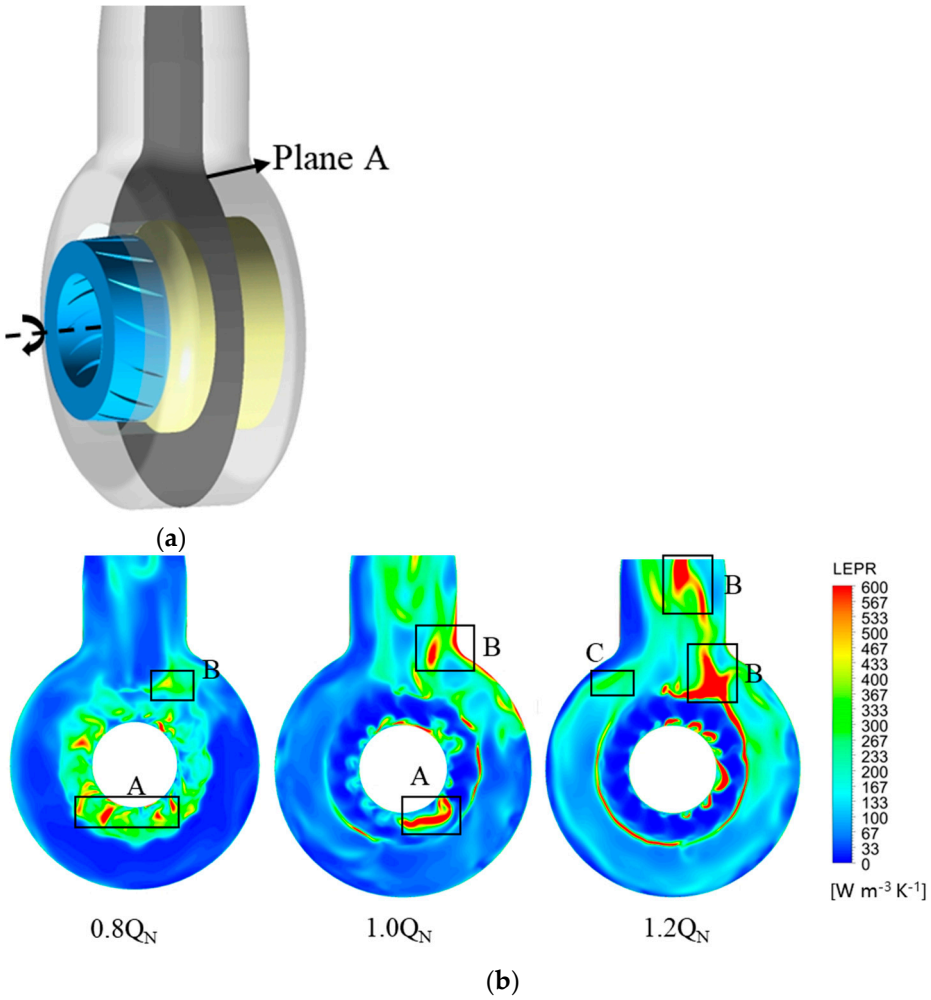

Figure 12. (**a**) Diagram of Plane A; (**b**) distribution of LEPR in plane A.

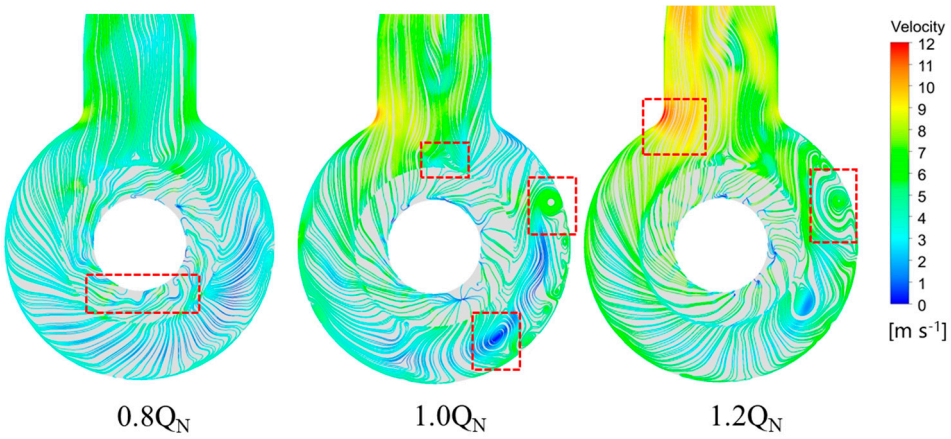

Figure 13. Streamlines diagram of Plane A under different flow rates.

Figure 14 shows the distribution of wall entropy production rate within the annular casing and diversion ring at different flow rates. As observed from the figure, regions of high wall entropy production rates are mainly concentrated near the discharge pipe, the volute tongue, and the annular wall regions. These high-entropy production areas are primarily caused by vortices with significant velocity gradients resulting from fluid impinging on the wall surfaces. Additionally, due to the wake flow of the guide vane blades, the inner wall of the diversion ring exhibits uniformly high wall entropy production rate regions.

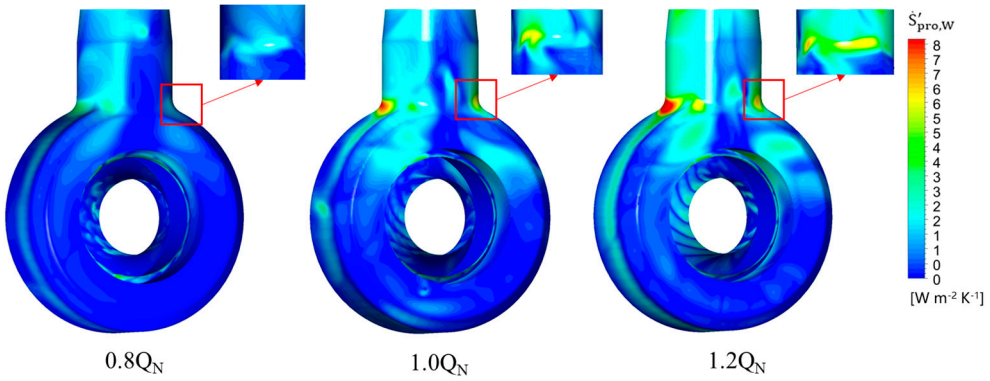

Figure 14. The wall entropy production rate in the annular casing and diversion ring.

6. Conclusions

This study focuses on the hydraulic model of the axial-flow RCP and analyzes the distribution characteristics of flow losses in different flow regions within the RCP and the hydraulic causes. The main research findings are as follows:

(1) The experimental results of the performance parameters of the RCP are generally consistent with the trends of numerical simulation results. The maximum errors in head and efficiency are 5.8% and 3.4% respectively, indicating the reliability of the numerical methods employed in this study.

(2) Analysis of the entropy production characteristics of different hydraulic components within the RCP reveals that turbulent entropy production contributes the most to the total entropy production, accounting for over 70% in all operating conditions; while direct entropy production contributes the least, at less than 10%. The impeller and annular casing are the primary components causing energy losses; with hydraulic losses accounting for 38.9% within the impeller and 43.3% within the annular casing at $1.0Q_N$.

(3) The analysis of energy loss within the impeller and guide vane shows that high local entropy production areas are mainly concentrated on the suction surface of the impeller blades and the leading edge and wake regions of the guide vane blades. At the same flow rate, the high local entropy production area near the shroud is significantly larger than that near the hub. At the 0.95Span section near the shroud, tip clearance leakage flow and flow separation are the primary causes of energy dissipation.

(4) The differences in flow structures within the annular casing under different operating conditions are significant. At $0.8Q_N$, energy losses in the symmetrical regions of the casing are nearly equal. With increasing flow rate, the number and scale of vortices inside the annular casing increase significantly, and are mainly concentrated in the right volute tongue and discharge pipe regions.

In conclusion, these research findings provide specific optimization targets for the subsequent development of axial-flow RCP hydraulic models. Engineers can develop targeted strategies to enhance pump performance and reliability, such as adjusting the blade tip clearance size, optimizing the matching relationship between the diversion ring and annular casing, and enlarging the throat area of the annular casing.

Author Contributions: Methodology, D.N.; validation, Z.L.; data processing, Y.S.; resources, W.G.; supervision, B.G. All authors have read and agreed to the published version of the manuscript.

Funding: This work is funded by the National Natural Science Foundation of China, No.52376024, China Post-doctoral Science Foundation, No.2017M611722, Project supported by Jiangsu postdoctoral research fund, No.1701054B, the Fundamental Science Research Project of Jiangsu Higher Education Institutions, No.22KJB570002.

Data Availability Statement: The original contributions presented in the study are included in the article, further inquiries can be directed to the corresponding author.

Conflicts of Interest: The authors declare no conflicts of interest in the paper.

Nomenclature

Acronyms	
CFD	Computational Fluid Dynamics
PWR	Pressurized water reactor
RCP	Reactor coolant pump
NPP	Nuclear power plant
SST	Shear-Stress Transport
SS	Suction Side
PS	Pressure Side
LEPR	Local Entropy Production Rate
Symbols	
Q_N	Nominal flow rate, m^3/s
ψ_N	Nominal head coefficient
n	Nominal rotating speed, s^{-1}
n_s	Specific speed
D_2	Impeller outlet diameter, m
Z_i	Impeller blade number
Z_g	Guide vane blade number
P_S	Hydraulic loss obtained by the pressure drop method, W
P_E	Hydraulic loss obtained by the experiments, W
P	Shaft power, W
w	Angular velocity, rad/s
T	Shaft torque, N·m
μ	dynamic viscosity, $N{\cdot}s/m^2$
k	Turbulent kinetic energy, m^2/s^2
ω	Turbulent eddy viscosity frequency, s^{-1}

τ	Wall shear stress, Pa
ρ	Water density, kg/m^3
V	Passing through fluid volume, m^3
A	Passing through fluid area, m^2
$\dot{S}'_{pro,D}$	Total entropy production rate, W/m^3·K
$\dot{S}'_{pro,\overline{D}}$	Direct entropy production rate, W/m^3·K
$\dot{S}'_{pro,W}$	Wall entropy production rate, W/m^3·K
$\dot{S}'_{pro,T}$	Turbulent entropy production rate, W/m^3·K
$S_{pro,D}$	Total entropy production, W/K
$S_{pro,W}$	Wall entropy production, W/K
$S_{pro,\overline{D}}$	Direct entropy production, W/K
$S_{pro,T}$	Turbulent entropy production, W/K

References

1. Zhan, L.; Bo, Y.; Lin, T.; Fan, Z. Development and outlook of advanced nuclear energy technology. *Energy Strategy Rev.* **2021**, *34*, 100630. [CrossRef]
2. Gralla, F.; Abson, D.J.; Møller, A.P.; Lang, D.J.; Wehrden, H.V. Energy transitions and national development indicators: A global review of nuclear energy production. *Renew. Sustain. Energy Rev.* **2017**, *70*, 1251–1265. [CrossRef]
3. Gao, H.; Gao, F.; Zhao, X.; Chen, J.; Cao, X. Analysis of reactor coolant pump transient performance in primary coolant system during start-up period. *Ann. Nucl. Energy* **2013**, *54*, 202–208. [CrossRef]
4. Long, Y.; Wang, D.; Yin, J. Experimental investigation on the unsteady pressure pulsation of reactor coolant pumps with non-uniform inflow. *Ann. Nucl. Energy* **2017**, *110*, 501–510. [CrossRef]
5. Xu, R.; Long, Y.; Wang, D. Effects of rotating speed on the unsteady pressure pulsation of reactor coolant pumps with steam-generator simulator. *Nucl. Eng. Des.* **2018**, *333*, 25–44. [CrossRef]
6. Ye, D.; Lai, X.; Chen, J.; Zhai, F.; Wu, J.; Gou, Q. Fluid Energy Conversion Analysis in Hydraulic Channels of reactor coolant pump under flow coastdown transient. *Energy Rep.* **2022**, *8*, 9232–9241. [CrossRef]
7. Ye, D.; Lai, X.; Luo, Y.; Liu, A. Diagnostics of nuclear reactor coolant pump in transition process on performance and vortex dynamics under station blackout accident. *Nucl. Eng. Technol.* **2020**, *52*, 2183–2195. [CrossRef]
8. Tao, R.; Xiao, R.F.; Liu, W.C. Investigation of the flow characteristics in a main nuclear power plant pump with eccentric impeller. *Nucl. Eng. Des.* **2018**, *327*, 70–81. [CrossRef]
9. Lu, Y.; Wang, Z.; Zhu, R.; Wang, X.; Long, Y. Study on flow characteristics in LBE-cooled main coolant pump under positive rotating condition. *Nucl. Eng. Technol.* **2022**, *54*, 2720–2727. [CrossRef]
10. Ni, D.; Yang, M.G.; Zhang, N.; Li, Z. Unsteady flow structures and pressure pulsations in a nuclear reactor coolant pump with spherical casing. *J. Fluids Eng.-Trans.* **2017**, *139*, 051103. [CrossRef]
11. Ni, D.; Yang, M.; Gao, B.; Zhang, N.; Li, Z. Experimental and numerical investigation on the pressure pulsation and instantaneous flow structure in a nuclear reactor coolant pump. *Nucl. Eng. Des.* **2018**, *337*, 261–270. [CrossRef]
12. Yu, S.; Song, H. Influence mechanism of the non-uniform inflow on performance of reactor coolant pump. *Ann. Nucl. Energy* **2023**, *180*, 109467. [CrossRef]
13. Gu, Y.; Pei, J.; Yuan, S.Q.; Wang, W.J.; Zhang, F.; Wang, P.; Appiah, D.; Liu, Y. Clocking effect of vaned diffuser on hydraulic performance of high-power pump by using the numerical flow loss visualization method. *J. Energy* **2019**, *170*, 986–997. [CrossRef]
14. Wang, C.; Zhang, Y.X.; Yuan, Z.Y.; Ji, K.Z. Development and application of the entropy production diagnostic model to the cavitation flow of a pump-turbine in pump mode. *J. Renew. Energy* **2020**, *154*, 774–785. [CrossRef]
15. Wang, C.; Zhang, Y.X.; Hou, H.C.; Yuan, Z.Y.; Liu, M. Optimization design of an ultra-low specific-speed centrifugal pump using entropy production minimization and taguchi method. *J. Int. J. Fluid Mach. Syst.* **2020**, *13*, 55–67. [CrossRef]
16. Rajeh, T.; Al-kbodi, B.H.; Zayed, M.E.; Li, Y.; Zhao, J.; Rehman, S. Local entropy generation optimization and thermodynamic irreversibility analysis of oval-shaped coaxial ground heat exchangers: A detailed numerical investigation. *Int. J. Heat Mass Transf.* **2024**, *228*, 125650. [CrossRef]
17. Wang, X.; Wang, Y.; Liu, H.; Xiao, Y.; Jiang, L.; Li, M. A numerical investigation on energy characteristics of centrifugal pump for cavitation flow using entropy production theory. *Int. J. Heat Mass Transf.* **2023**, *201*, 123591. [CrossRef]
18. Ji, L.; Li, W.; Shi, W.; Tian, F.; Agarwal, R. Diagnosis of internal energy characteristics of mixed-flow pump within stall region based on entropy production analysis model. *Int. Commun. Heat Mass Transf.* **2020**, *117*, 104784. [CrossRef]
19. Yang, G.; Shen, X.; Shi, L.; Zhang, D.; Zhao, X. Numerical investigation of hump characteristic improvement in a large vertical centrifugal pump with special emphasis on energy loss mechanism. *Energy* **2023**, *273*, 127163. [CrossRef]
20. Li, P.; Lu, J.; Tao, R.; Xiao, R.; Ji, B.; Wang, F. Energy distribution and chaotic pressure pulsation analysis of vortex ropes in Francis-99. *Eng. Appl. Comput. Fluid Mech.* **2024**, *18*, 2310609. [CrossRef]
21. Zhang, Y.; Zheng, S.; Zhao, Y. Numerical investigation of flow characteristics in the front and rear chambers of centrifugal pump and pump as turbine. *Sci. Rep.* **2024**, *14*, 11955. [CrossRef]

22. Sun, S.; Sun, J.; Song, P.; Wang, S. Flow Investigation and Optimization Design of a Radial Outflow Liquid Turbine Expander for Liquid CO_2 Energy Storage System. *J. Fluids Eng.* **2024**, *146*, 041201. [CrossRef]
23. Afridi, M.I.; Chen, Z.M.; Qasim, M.; Makinde, O.D. Computational analysis of entropy generation minimization and heat transfer enhancement in magnetohydrodynamic oscillatory flow of ferrofluids. *J. Magn. Magn. Mater.* **2024**, *594*, 171848. [CrossRef]
24. Liu, H.; Xia, R.; Wang, K.; Jing, Y.; He, X. Experimental Analysis on Pressure Fluctuation Characteristics of a Centrifugal Pump with Vaned-Diffuser. *Water* **2020**, *12*, 126. [CrossRef]
25. Menter, F.R. Two Equation Eddy Viscosity Turbulence Models for Engineering Applications Sstkw. *AIAA J.* **1994**, *32*, 1598–1605. [CrossRef]
26. He, J.W.; Si, Q.R.; Sun, W.T.; Liu, J.F.; Miao, S.C.; Wang, X.H.; Wang, P.; Wang, C.G. Study on the energy loss characteristics of ultra-low specific speed PAT under different short blade lengths based on entropy production method. *Energy* **2023**, *283*, 129026. [CrossRef]
27. Kock, F.; Herwig, H. Local entropy production in turbulent shear flows: A high-reynolds number model with wall functions. *J. Int. J. Heat Mass Transf.* **2004**, *47*, 2205–2215. [CrossRef]
28. Mathieu, J.; Scott, J. *An Introduction to Turbulent Flow*; Cambridge University Press: Cambridge, UK, 2000.
29. Lin, T.; Li, X.J.; Zhu, Z.C.; Xie, J.; Li, Y.; Yang, H. Application of enstrophy dissipation to analyze energy loss in a centrifugal pump as turbine. *Renew. Energy* **2021**, *163*, 41–55. [CrossRef]